Enhanced plasmonic photocatalytic performance of C_3N_4/Cu by the introduction of reduced graphene oxide interlayer

Qixiao Gai[a,b], Shoutian Ren[a*], Xiaochun Zheng[a,b], Wenjun Liu[a*]

[a] Department of Optoelectronic Science, Harbin Institute of Technology at Weihai, Weihai 264209, People's Republic of China

[b] Department of Physics, Harbin Institute of Technology, Harbin 150001, People's Republic of China

[*]Corresponding author:

E-mail address: renst77@163.com; liuwenjun86@163.com

Table of contents

Fig. S1 (a) TEM image and (b) N_2 adsorption-desorption isotherm distribution of PCN, and (c) TEM and (d) HRTEM images of PCN/RGO.

Fig. S2 (a)TEM image, (b-d) element mapping distribution of PCN/23Cu. Cu NPs are marked with red circles in panel (a), and the insets in panel (b) correspond to the detected sample.

Fig. S3 (a) TEM and (b) HRTEM images of PCN/RGO/20Cu/Pt.

Fig. S4 FT-IR spectra of (a) GO and (b) PCN/RGO/25Cu.

Fig. S5 Survey-level scan XPS spectra of PCN/RGO, PCN/RGO/20Cu.

Fig. S6 (a) Tauc plots of PCN, (b) absorption spectra of RGO and Cu NPs extracted by the absorption difference between PCN/RGO and PCN and the absorption difference between PCN/RGO/xCu and PCN/RGO, respectively, (c) M-S plots of PCN and PCN/RGO.

Table S1 Zeta potential values of PCN, GO and PCN/RGO.

Fig. S7 (a) XRD and (b) FT-IR spectra of CN and PCN.

Fig. S8 Calculated Fermi levels of (a) C_3N_4 (002), (b) RGO (002) and (c) Cu (111).

Fig. S9 Schematic diagrams of PCN/RGO/Cu heterojunction: IEF induced charge transfer and separation.

Fig. S10 Time courses of photocatalytic hydrogen production of (a) PCN, PCN/RGO, PCN/23Cu, different PCN/RGO/Cu and (b) PCN/RGO/20Cu with CH_3OH and without CH_3OH and (c) PCN/RGO/20Cu/Pt and PCN/RGO/Pt.

Fig. S11 XRD patterns of PCN/RGO/20Cu before and after photoreaction.

Fig. S12 Orbital distribution of RGO/Cu composites in the highest oscillator strength transition state (a) before and (b) after excitation, respective.

Table S2 Entries in the table are fitted from EIS results.

Fig. S13 The band structures of (c) C_3N_4, (d) CN/Cu and (e) CN/RGO/Cu

Fig. S14 Colormap surface with projection of the electromagnetic field distributions of (a) PCN/Cu and (b) PCN/RGO/Cu under linear plane wave illumination.

Fig. S15 Charge difference density of PCN/RGO and RGO/Cu.

Table S3 Total Mulliken charge populations of PCN/RGO, WPCN/RGO, RGO/Cu and WRGO/Cu.

Fig. S16 The partial density of states of different sites.

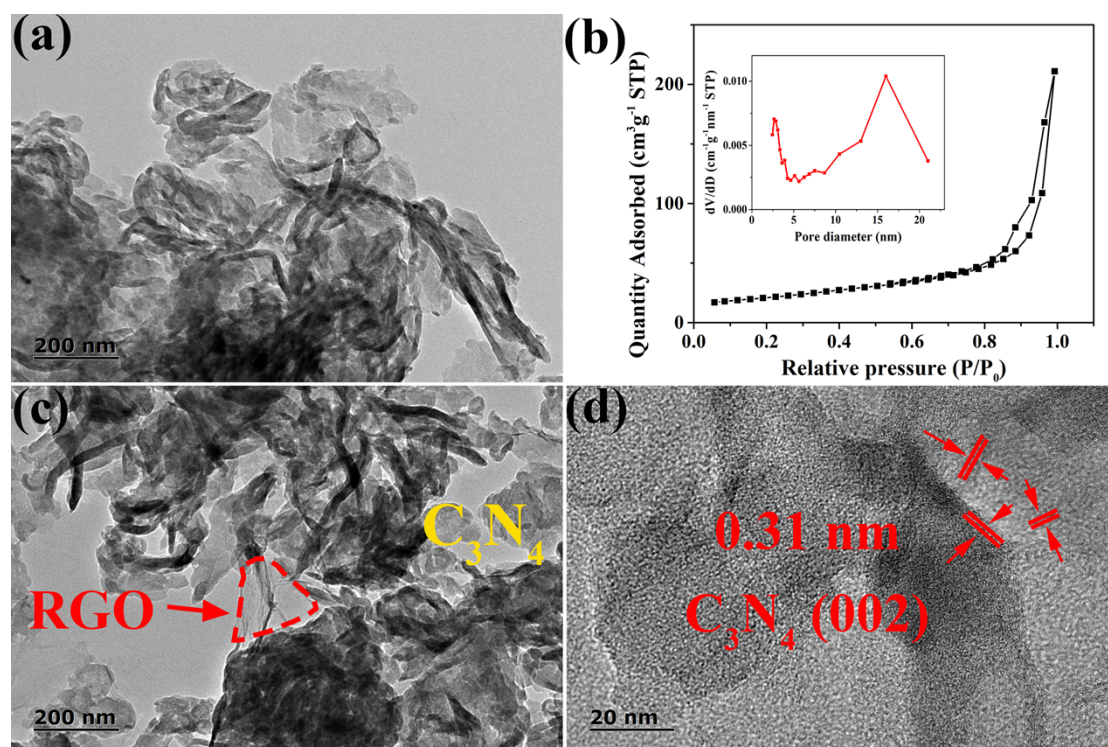**Fig. S17** Gibbs free energy for hydrogen adsorption on CN/RGO/Cu and CN/Cu.

Fig. S1 (a) TEM image and (b) N_2 adsorption-desorption isotherm distribution of PCN, and (c) TEM and (d) HRTEM images of PCN/RGO. The insets in panel (b) correspond to the corresponding pore diameter distribution of PCN.
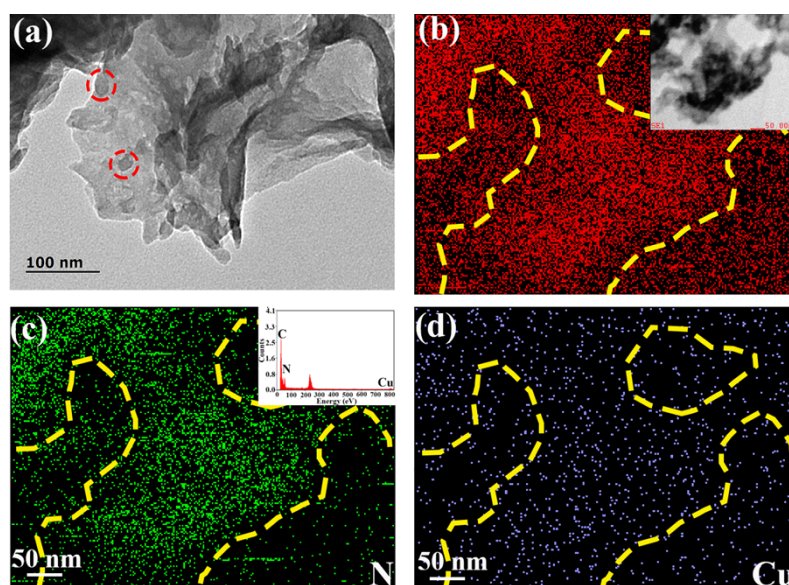

Fig. S2 TEM image (a) and element mapping distribution (b-d) of PCN/23Cu. Cu NPs are marked with red circles in panel (a), and the insets in panel (b) and (C) correspond to the detected sample and EDS result, respectively.
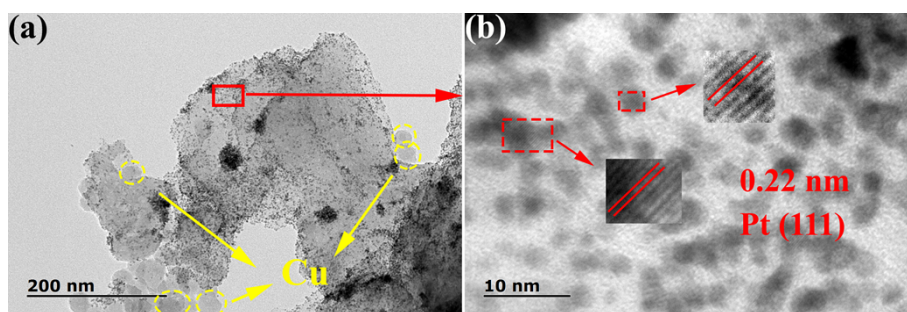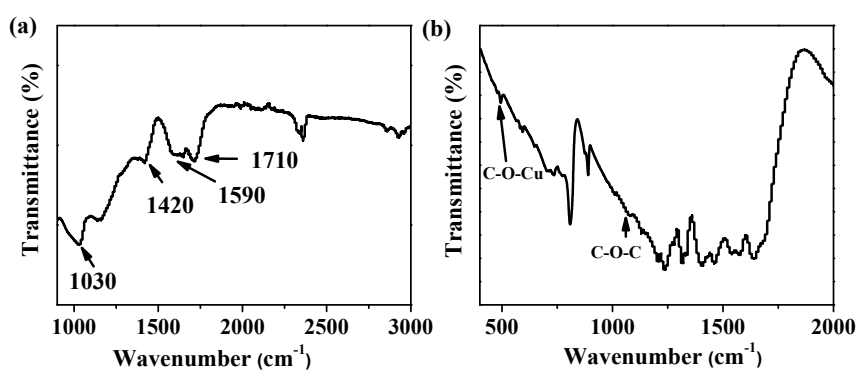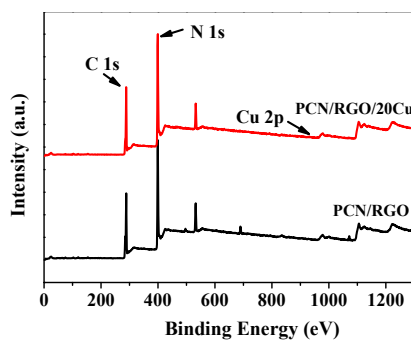
Fig. S3 (a) TEM and (b) HRTEM images of PCN/RGO/20Cu/Pt. Cu NPs are marked with yellow circles in panel (a). The insets in panel (b) correspond to the enlarged view of the lattice spacing of Pt.

Fig. S4 FT-IR spectra of (a) GO and (b) PCN/RGO/25Cu.

Fig. S5 Survey-level scan XPS spectra of PCN/RGO and PCN/RGO/20Cu.
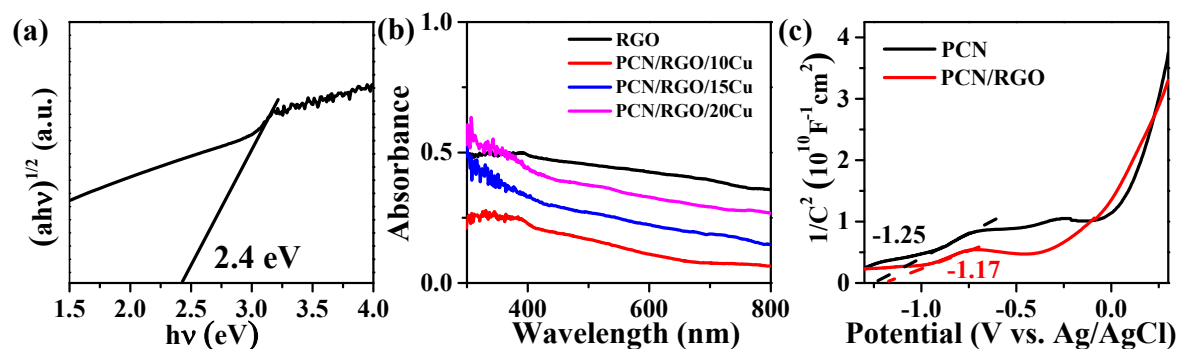
Fig. S6 (a) Tauc plots of PCN, (b) absorption spectra of RGO and Cu NPs extracted by the absorption difference between PCN/RGO and PCN and the absorption difference between PCN/RGO/xCu and PCN/RGO, respectively, (c) M-S plots of PCN and PCN/RGO.

Table S1 Zeta potential values of PCN, GO and PCN/RGO.

Potential value (mV) / Number \ Catalyst	PCN	GO	PCN/RGO
1	6.17	-39.60	-0.93
2	7.49	-43.70	-0.67
3	9.81	-38.70	-1.60
Average	7.82	-40.67	-1.07

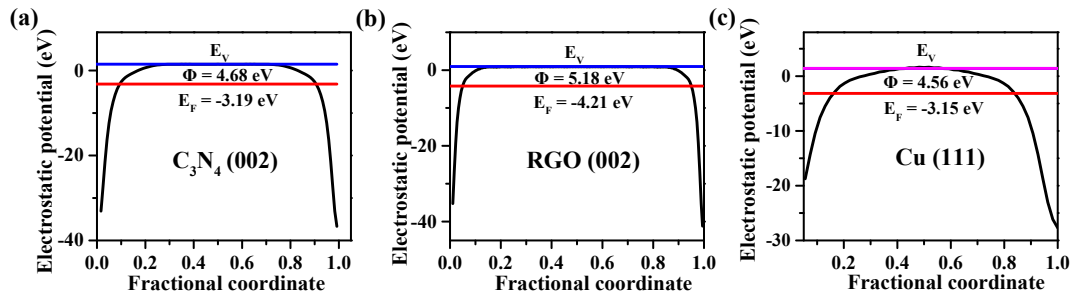Fig. S7 (a) XRD and (b) FT-IR spectra of CN and PCN.

Fig. S8 Calculated Fermi levels of (a) C_3N_4 (002), (b) RGO (002) and (c) Cu (111).
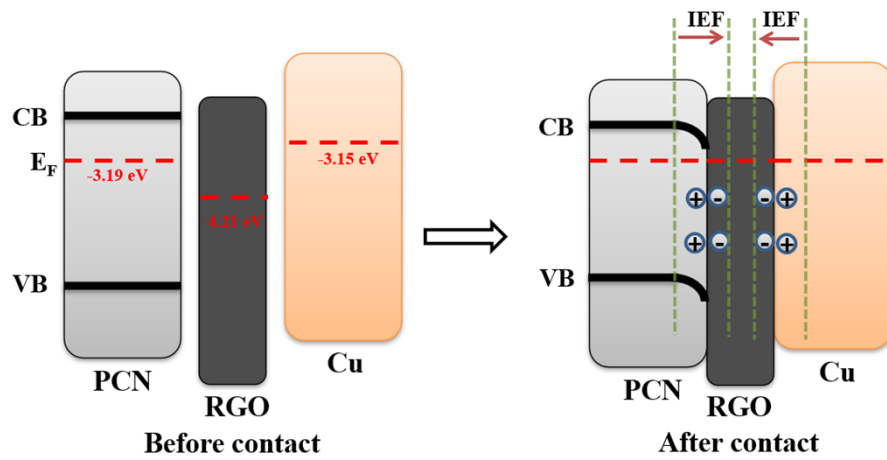

Fig. S9 Schematic diagrams of PCN/RGO/Cu heterojunction: IEF induced charge transfer and separation.
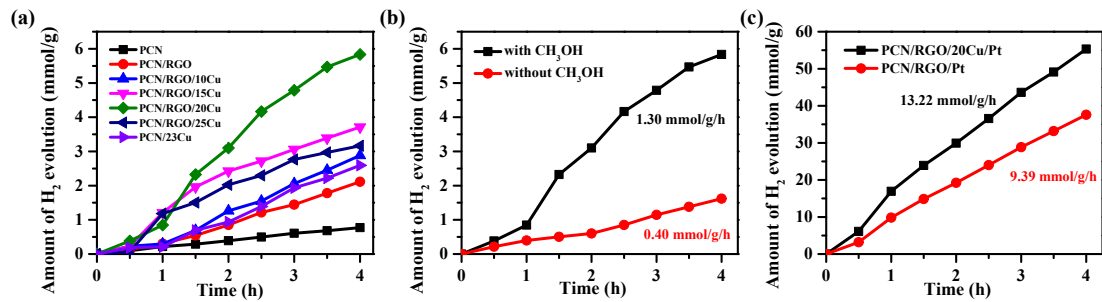

Fig. S10 Time courses of photocatalytic hydrogen production of (a) PCN, PCN/RGO, PCN/23Cu, different PCN/RGO/Cu and (b) PCN/RGO/20Cu with CH_3OH and without CH_3OH and (c) PCN/RGO/20Cu/Pt and PCN/RGO/Pt.
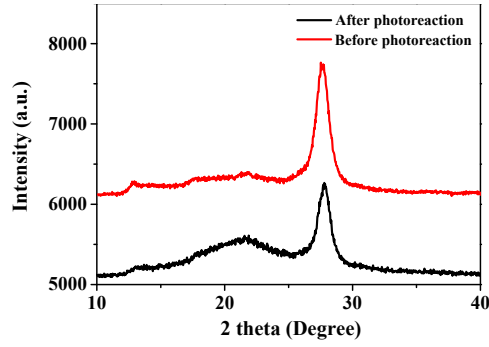
Fig. S11 XRD patterns of PCN/RGO/20Cu before and after photoreaction.
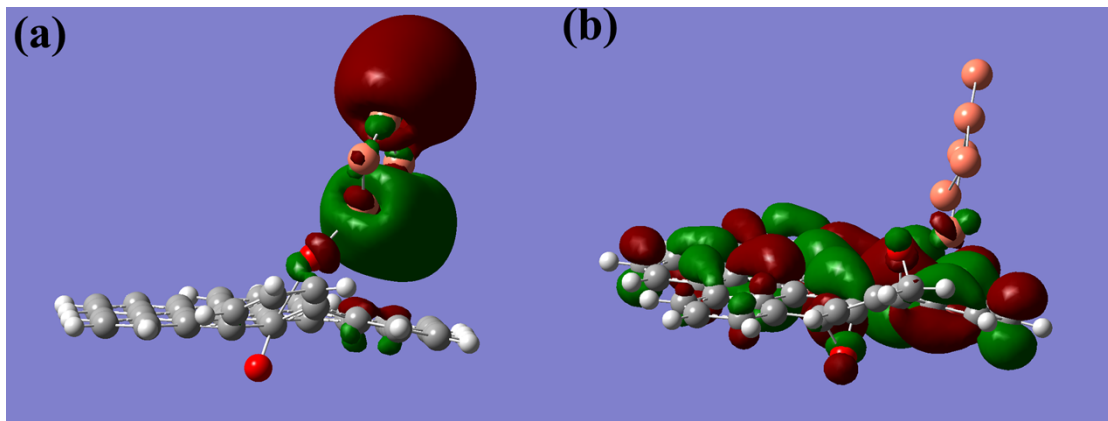

Fig. S12 Orbital distribution of RGO/Cu composites in the highest oscillator strength transition state (a) before and (b) after excitation, respective. The green and red parts are orbital wave functions

Table S2 Entries in the table fitted from EIS results (Fig.7a).

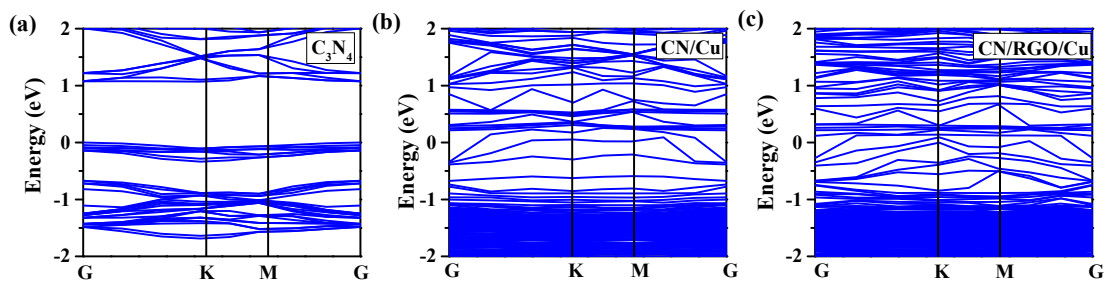| Samples	PCN	PCN/RGO	PCN/23Cu	PCN/RGO/20Cu
R_s (Ω)	0.25	0.28	0.31	0.26
R_{ct} (Ω)	1213.0	946.5	659.4	209.1

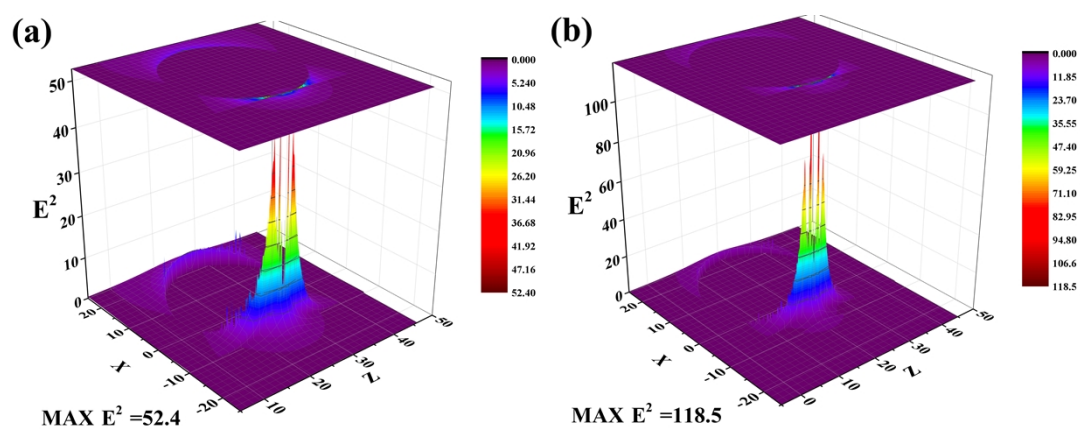Fig. S13 The band structures of (c) C_3N_4, (d) CN/Cu and (e) CN/RGO/Cu

Fig. S14 Colormap surface with projection of the electromagnetic field distributions of (a) PCN/Cu and (b) PCN/RGO/Cu under linear plane wave illumination.
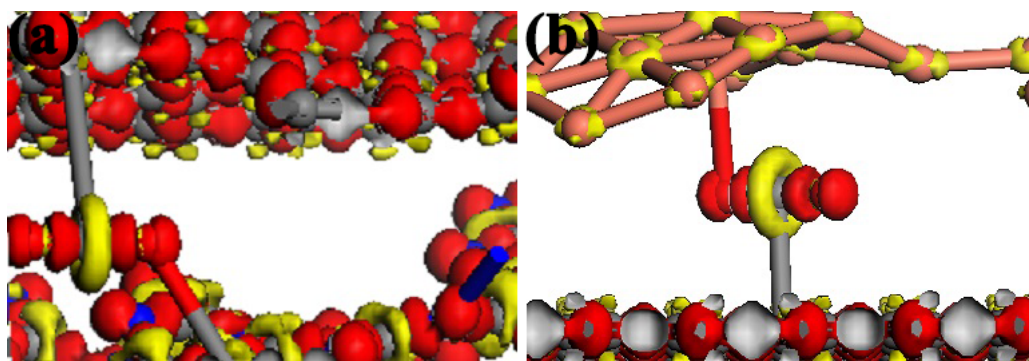

Fig. S15 Charge difference density of PCN/RGO and RGO/Cu. The red and yellow regions represent electron enrichment and depletion regions, respectively.

Table S3 Total Mulliken charge populations of PCN/RGO, WPCN/RGO, RGO/Cu and WRGO/Cu.

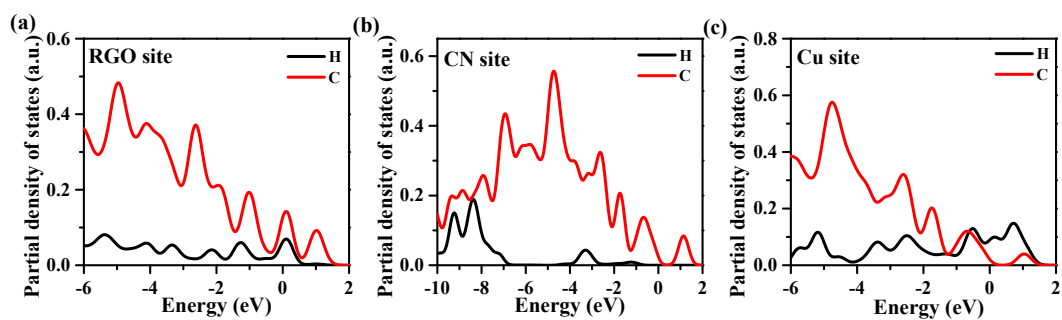|	SUM PCN (e)	SUM RGO (e)	SUM Cu (e)
PCN/RGO	-0.46	0.44	
WPCN/RGO	-0.03	0.06	
RGO/Cu		-0.33	0.38
WRGO/Cu		-0.25	0.31

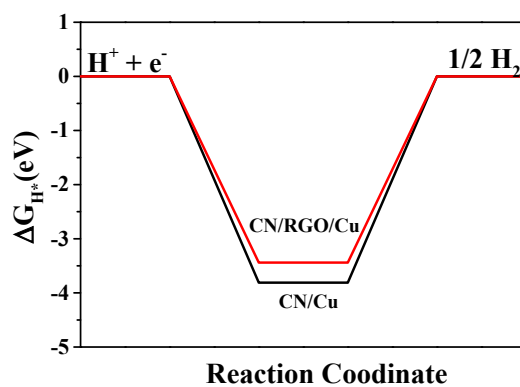Fig. S16 The partial density of states of different sites.

Fig. S17 Gibbs free energy for hydrogen adsorption on CN/RGO/Cu and CN/Cu.